Letter

Observation of optical tunneling inhibition by a parabolic potential in twisted photonic lattices

Weijie Liu, Bin Zhang, Bo Wu, Lei Wang, and Feng Chen*

School of Physics, State Key Laboratory of Crystal Materials, Shandong University, Jinan 250100, People's Republic of China

(Received 5 August 2021; accepted 19 March 2022; published 31 March 2022)

Quantum tunneling is considered the cornerstone of many physical processes. So far, its evolution over time, especially under an external field superimposed on the periodic potential field, has not been directly observed experimentally due to the harsh requirements and extremely short time scale. In this paper, we fabricate twisted photonic lattices consisting of three-dimensional waveguide arrays and experimentally illustrate the optical tunneling process under the parabolic potential field through the photonic route. Optical tunneling inhibition is observed experimentally, and the reduced time required to achieve the maximum transfer of waveguides indicates the inhibition can be modulated by the parabolic potential. This provides a reliable means for subsequent experimental study of quantum tunneling under complicated external potential field.

DOI: 10.1103/PhysRevResearch.4.L012043

Quantum tunneling is the basis of many interesting physical phenomena [1]. Imposing small disturbances on the periodic potential (e.g., a time-harmonic drive or defects) can achieve either strong inhibition or enhancement [2–4]. Control of quantum tunneling has been reported in different areas of physics, such as ultracold atoms in optical lattices, multiquantum dots, and spin systems [5,6]. However, due to the influence of many-body effects, decoherence, thermal motion, and nonlinear terms in experiments, complex and harsh conditions are usually required to observe the expected quantum phenomena [7,8]. In addition, the wave function following the Schrödinger equation evolves very quickly with time; the stable states rather than the dynamic evolution are usually observed in the quantum tunneling process.

The photonic lattice is a unique system for investigating abundant phenomena of physical portfolios [9–16]. For examples, the engineered photonic lattices have been utilized to study Bloch oscillations, Anderson localizations, dynamic localizations, Aharonov-Bohm (AB) effects, flat-band states, and topological insulators [3,17–20] in optical domains. The longitudinal modulation is crucial to engineer the light behaviors in photonic lattices, but the overall three-dimensional (3D) longitudinal modulation is still lacking in experiments [21–32]. Previous theoretical study predicted that the light evolution in the twisted photonic lattice, a suitable platform to achieve longitudinal modulation, resembles optical tunneling under a parabolic potential field [10], which opens a conceivable route to study optical tunneling under the external field. Nevertheless, the experimental demonstration with detailed dynamic process of optical tunneling under the parabolic potential field is lacking. Particularly, from the fabrication point of view, the twisted photonic lattices require waveguides with high hopping symmetry, which is difficult to fabricate experimentally.

In this paper, we demonstrate experimental evidence for the light evolutionary behavior of optical tunneling under a parabolic potential field using a twisted photonic lattice consisting of 3D rotating waveguides with high hopping symmetry. We use the twisted modulation as a parabolic potential after coordinate frame transformation, in which the strength of the parabolic potential is determined by the distance from the rotating center and the twisting rate. The experimental results are consistent with the numerical calculation. In addition to the expected optical tunneling inhibition by the parabolic potential, we also observe experimentally the fast dynamic evolution of the tunneling. As the parabolic potential increases to a certain extent, we have experimentally obtained almost localized optical propagation.

We start by considering a twisted photonic lattice where the waveguides rotate at a constant rate $\varepsilon = 2\pi/\Lambda$ around the center, as shown in Fig. 1(a). The waveguide array is arranged along the x direction. Here, Λ represents the spatial pitch associated with the helical structure. In a rotating reference frame (x, y, z) where $x = X\cos(\varepsilon z) + Y\sin(\varepsilon z)$, $y = -X\sin(\varepsilon z) + Y\cos(\varepsilon z)$, and $z = Z$, the propagation of the electric field envelop with the weak guidance approximation satisfies the Schrödinger-like wave equation [10]:

$$i\lambda\frac{\partial\psi}{\partial z} = -\frac{\lambda^2}{2n_s}\nabla^2\psi + V(x,y)\psi - \frac{n_s\varepsilon^2}{2}x^2\psi, \qquad (1)$$

where $\lambda = \lambda/2\pi$ represents the reduced wavelength, n_s is the substrate refractive index, and $V(x,y) = \sum_n[n_s - n_g(x-na, y)]$ denotes the periodic optical potential where $n_g(x,y)$ is the index profile of the single waveguide, and a is the distance between centers of adjacent waveguides. Equation (1) is analogous to the ultracold atomic wave function in amplitude-modulated parabolic optical lattices [33–36]. This suggests the twisted photonic lattice is a planar photonic

*drfchen@sdu.edu.cn

Published by the American Physical Society under the terms of the Creative Commons Attribution 4.0 International license. Further distribution of this work must maintain attribution to the author(s) and the published article's title, journal citation, and DOI.

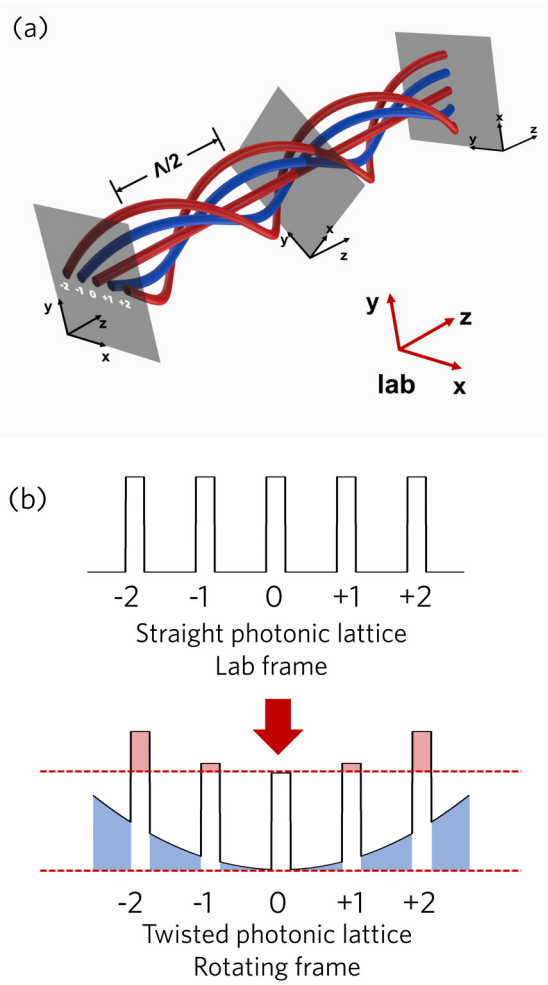


FIG. 1. (a) Schematic of the twisted photonic lattice. The lattice rotates around the 0 site. Axes are shown in the laboratory (red) and rotating (black) frames. (b) Top: Refractive potential distribution of the cross-section of the straight photonic lattice in the laboratory frame. Bottom: Refractive potential distribution of the cross-section of the twisted photonic lattice in the rotating frame.

lattice superimposed with a parabolic potential field. By considering ψ as the superposition of waveguide modes ψ_n with amplitudes c_n and $\psi = \sum_n c_n \psi_n$, the modal amplitudes c_n are calculated from the eigenvalue equation [10]:

$$i\frac{dc_n}{dz} = -\Delta(c_{n+1} + c_{n-1}) - \gamma n^2 c_n, \qquad (2)$$

where Δ is the hopping rate between adjacent sites. The second term on the right side of the Eq. (2) is due to the twisting, and $\gamma = \varepsilon^2 n_s a^2 / 2\lambda$.

To investigate optical tunneling in the parabolic potential field, we propose a scheme as illustrated in Fig. 1(b). It should be noted that, for convenience, we consider the distribution of the refractive index in the potential barriers as a constant value, which does not conform with the principle of superposition. However, from the obtained experimental data, the light forms a stable mode in the waveguide of the photonic lattice, which does not affect the demonstration of the fundamental physics. According to the scheme in Fig. 1(b), there are two significant changes in the potential distribution of a

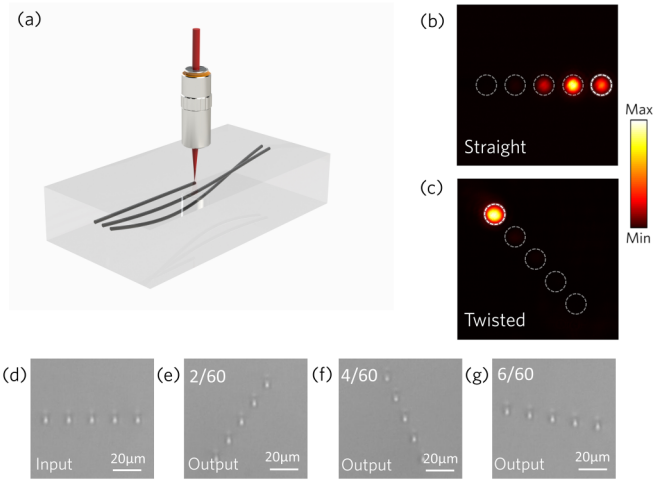


FIG. 2. (a) Schematic of fabricating twisted photonic lattices. (b) and (c) Experimental results of output intensity profiles in straight and twisted photonic lattices, respectively. Five dotted circles indicate the layout of the sites at the output. The excited site is marked by dotted bright circles. Compared with (b), the lattice in (c) rotates about 240° clockwise. (d)–(g) Optical micrograph of the facet of the twisted photonic lattice with five waveguides. (d) is the input facet and (e)–(g) are output facets with different rotating rates. Due to the different imaging principles, the arrangement direction of the waveguide array in the optical micrograph is mirror symmetrical with the arrangement direction in the intensity profiles.

twisted photonic lattice. First, the potential between adjacent sites becomes different, which expands with the increase of the parabolic potential [shown in red shadow in Fig. 1(b)]. This causes the eigenvalue β_n of the modes at different sites to become different, so that the light cannot be completely transferred from one to another lattice position after passing through the coupling length L_c. Due to the characteristics of the parabolic potential field, the farther away from the center of the parabola, the more obvious the phenomenon of the inhibition of optical tunneling will be observed. Second, the parabolic potential field makes the potential well between the sites filled to some extent [shown in blue shadow in Fig. 1(b)]. This will make the effective well depth smaller and induce the increment in the hopping rate, resulting in a reduction of the coupling length. Since the effect of the parabolic potential field on optical tunneling is related to the structure of the photonic lattice, one can use $g = \gamma/\Delta$ to scale the influence of the parabolic potential field, where Δ represents the effect of the photonic lattice, and γ represents the effect of the parabolic potential field.

The structure of the photonic lattice in this paper is illustrated in Fig. 1(a). The array twists at a constant rate around the 0 site. Five waveguides are arranged at equal intervals $a \sim 15\,\mu$m. The width of the fabricated waveguide is $\sim 4\,\mu$m, and the refractive index difference obtained by the simulation is $\Delta n \sim 10^{-3}$. Twisted photonic lattices are fabricated using direct femtosecond laser writing [12,35,36], as shown in Fig. 2(a). The borosilicate glass (Eagle XG) [37,38] is mounted on a 3D x-y-z translation stage. A femtosecond laser at wavelength of 1030 nm, pulse duration of 400 fs, and repetition rate of 2.5 MHz is used as the light source.

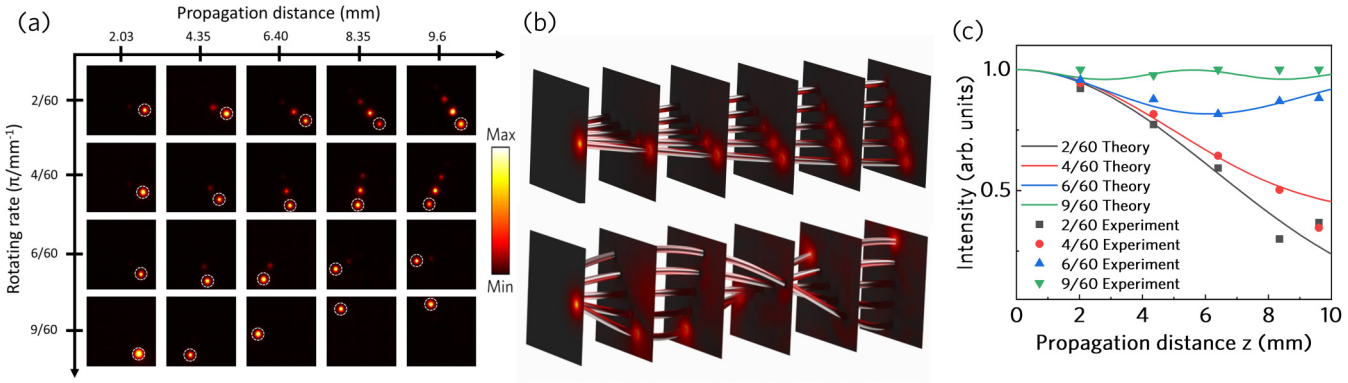


FIG. 3. (a) Experimental results of output intensity profiles in twisted photonic lattices with different propagation distances and rotating rates. White dotted circles are the excited sites. (b) Simulation results with high ($\frac{9}{60}\,\pi$/mm) and low ($\frac{2}{60}\,\pi$/mm) rotating rates, respectively. Light intensity profiles correspond to the propagation distance of 0, 2, 4, 6, 8, and 10 mm, respectively. (c) Normalized light intensity at the output of excited sites of (a) (see Appendix E for detailed data). Theoretical results corresponding to the same set of parameters are provided for comparison.

A microscope objective ($\frac{50}{0.45}$) is utilized to focus the laser beam into the borosilicate glass at the depth of $\sim$230 μm. Because the photonic lattice is twisted, the light may tunnel in any direction, and the fabricated waveguides must possess good hopping symmetry. By carefully selecting fabricating parameters, the waveguides that satisfy the requirement for hopping symmetry have been produced (see Appendix A). It is worth noting that, since the femtosecond laser is incident from the upper surface and one waveguide needs to be fabricated continuously at a time, for these twisted photonic lattices, the rotation angle of a single waveguide cannot exceed 270°. Figure 2(d) shows the optical microscope image of the photonic lattice as a cross-section of the sample (i.e., the incident facet). As an example, Figs. 2(e)–2(g) show the microscope images of the 9.6 mm photonic lattices at the output facets under different rotating rates. We keep the photonic lattice at the input facet arranged horizontally, and the arrangement of the photonic lattice at the output facet will change with the length and rotation rate. Along the direction of light propagation, the photonic lattice rotates clockwise, as depicted in Fig. 1(a). In addition, the spatial pitch Λ of the helixes is larger than $\sim$3 orders of magnitude over the lattice interval corresponding to the radius of the helixes. Therefore, the curvature of the waveguide structure is very small, and the light is well confined in the waveguide. The propagation behaviors of light are characterized by the end-face coupling system at a wavelength of 633 nm. Figures 2(b) and 2(c) show the output patterns without and with parabolic potentials. The length of light propagation is 9.6 mm, and the light is excited from the $+2$ site. An obvious inhibition of optical tunneling is observed as the lattice is twisted.

To investigate the influence of parabolic potential field on optical tunneling in more detail, we first design a nontwisted two-waveguide system in which the fabricating parameters and interval are consistent with the twisted photonic lattice to measure Δ (see Appendix B). Since the spiral structure is of 3D geometry, it is impossible to use fluorescence microscopy to monitor the evolution of light propagation; therefore, photonic lattices of different lengths and rotation rates are used for exploration. The results are shown in detail in Fig. 3(a). The light is excited from the $+2$ site to obtain the most obvious phenomenon. As the rotating rate is relatively small, such as $\frac{2}{60}\,\pi$/mm, when the propagation distance increases, the light intensity at the $+2$ site gradually decreases, and the light intensity at the 0 and $+1$ sites increases. The intensity distribution after the light propagates 9.6 mm indicates that a large part of the light is at the 0 and $+1$ sites, which means that the optical tunneling behavior can still occur in the case of relatively small parabolic potential. With the increase of the rotating rate, optical tunneling will be significantly inhibited by the parabolic potential during the entire propagation process. For $\varepsilon = \frac{9}{60}\pi$/mm, there is no light intensity distribution at the other site, and optical tunneling is almost completely inhibited.

Figure 3(c) shows the comparison of the theoretical results solved by Eq. (2) and the corresponding experimental data. At the output facet, the light intensity at the site where the light is excited is used to indicate the degree of optical tunneling inhibition. From the theoretical results, all light is localized at the initial lattice site at the beginning. As z increases from 0 to 9.6 mm, obvious tunneling behavior occurs in the photonic lattice with weak rotating rate, the photonic lattice with high rotating rate makes the light intensity vibrate slightly at the initial lattice site, and most of the energy is always in the original lattice site. Generally, the complex phenomena of light propagating in the photonic lattice make it difficult to measure the time of a single tunneling behavior. For example, for $\varepsilon = \frac{2}{60}$ or $\frac{4}{60}\,\pi$/mm, the tunneling between the $+2$ and $+1$ sites and between the $+1$ and 0 sites are always mixed. However, as the potential field intensity increases and the light is mainly localized on the two waveguides ($+2$ and $+1$ sites), one can gradually observe the periodicity of the light intensity at the incident site with the propagation distance. For $\varepsilon = \frac{6}{60}$ and $\frac{9}{60}\,\pi$/mm, the periods are 12.6 and 5.6 mm, respectively. Further numerical calculations suggest that the length of the period can be modulated by the parabolic potential field, i.e., larger intensity of potential field induces a shorter period (see Appendix C). This periodicity of light intensity, like the two-waveguide system, can facilitate us to discuss the speed of optical tunneling. It is obvious that half of the period can represent the distance (or time) required for a tunneling process. Thus, the tunneling time for $\varepsilon = \frac{9}{60}\,\pi$/mm is 44% of

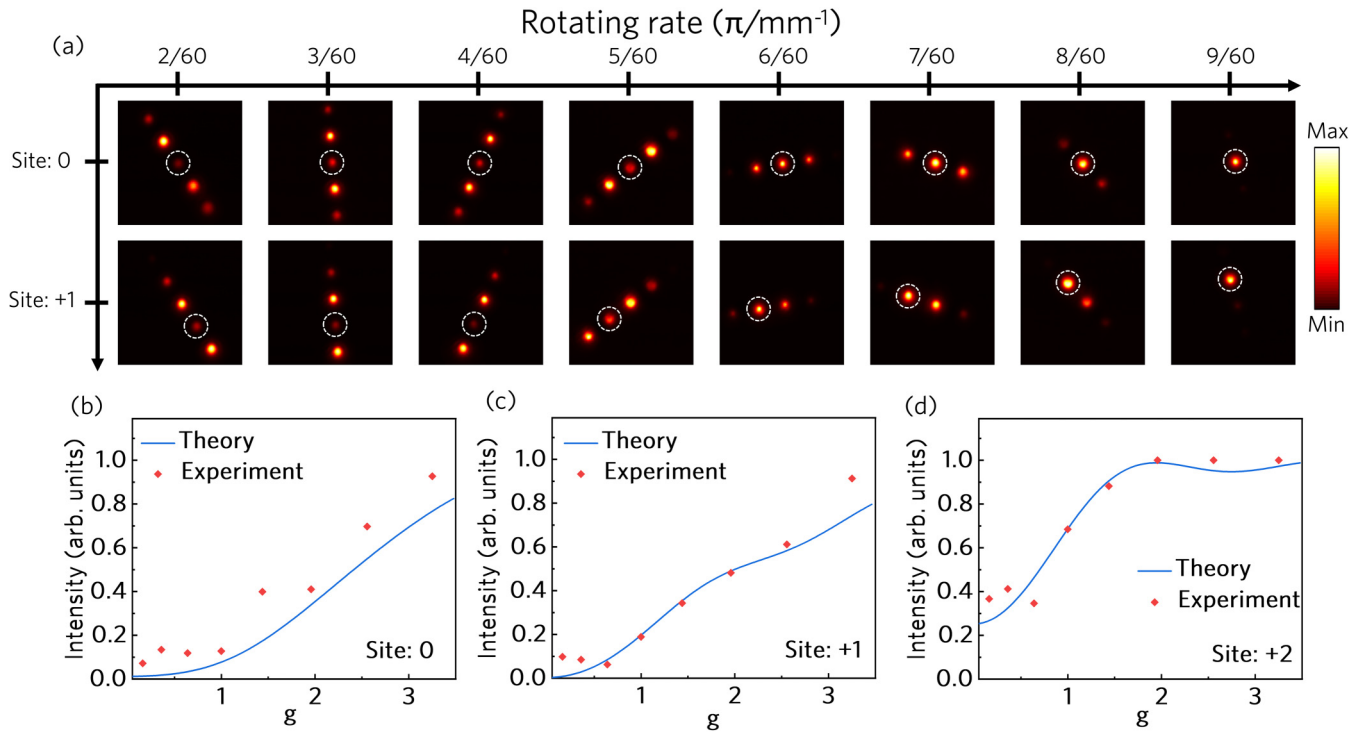


FIG. 4. (a) Output intensity profiles obtained in experiments with excited 0 and +1 sites. The dashed circles indicate the excited sites. (b)–(d) Normalized light intensity at the output of excited sites of (a): experimental (circles) and corresponding theoretical results (solid lines) (see Appendix E for detailed data).

that of the $\varepsilon = \frac{6}{60}\ \pi/\text{mm}$ case. Nevertheless, the theoretical and experimental results are in extremely good agreement with the scheme and clearly demonstrate parabolic-potential-induced tunneling inhibition. Figure 3(b) shows the results of the simulation using the beam propagation method. It shows the corresponding relationship between the end-face light intensity distribution and the photonic lattice structure. The bottom corresponds to the case where the rotating rate is $\frac{9}{60}\ \pi/\text{mm}$, and optical tunneling is completely inhibited. The top corresponds to the case where the rotating rate is $\frac{2}{60}\ \pi/\text{mm}$, and optical tunneling happens normally.

Next, we fix the lattice length at 9.6 mm and excite light from a different site to examine propagation proper-

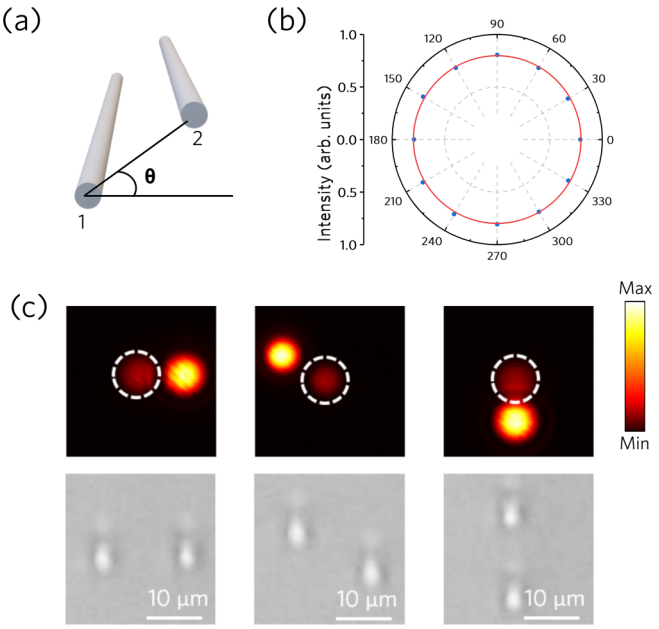


FIG. 5. (a) Schematic of the two-waveguide system. (b) The light intensity at the output end of the No. 2 waveguide with different arranged directions. (c) Top: Light intensity distribution obtained experimentally. Down: Optical micrograph of the input facet of the two-waveguide systems. The angles are 0°, 150°, and 270°, respectively.

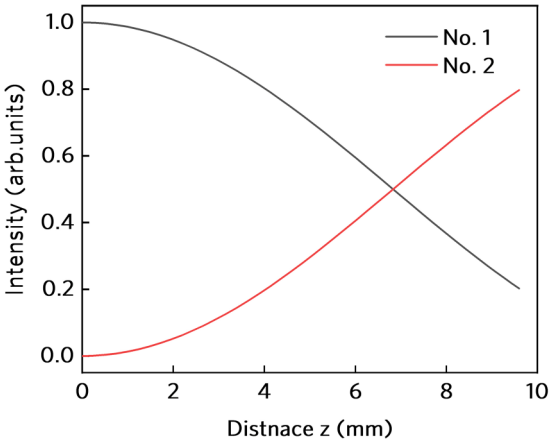


FIG. 6. The relationship between the light intensity and the propagation distance when the evanescent wave coupling occurs.

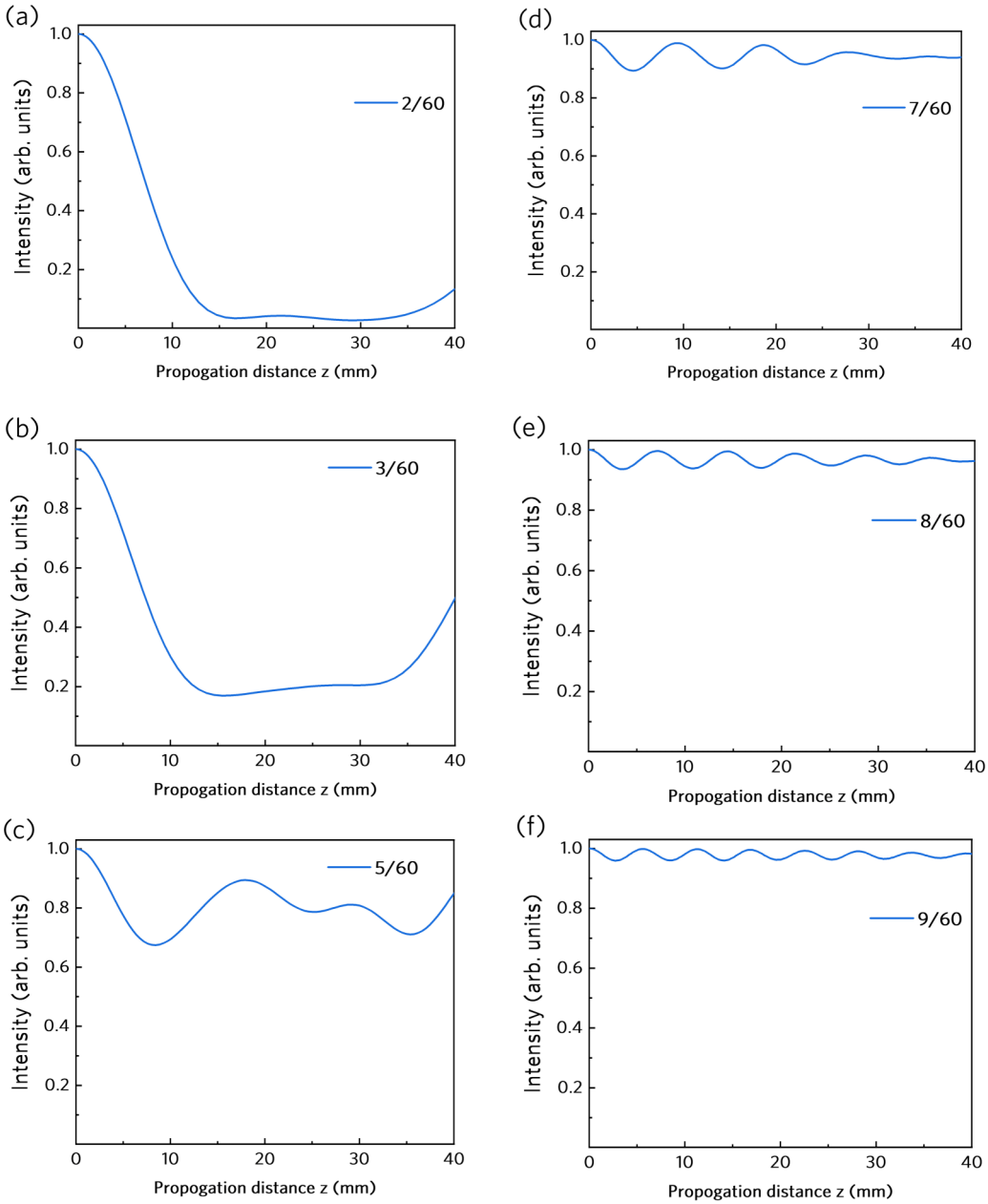


FIG. 7. Light intensity at the output of the excited +2 sites. (a)–(f) are with different rotating rates.

ties influenced by the geometric characteristic of parabola. The structure of the photonic lattice is the same as before. Figure 4(a) shows the results for exciting the photonic lattice from the 0 and +1 sites. We use g to measure the magnitude of the parabolic potential field, and Figs. 4(b)–4(d) indicate results where the output intensity from initial site is plotted against g. In these figures, the expected theoretical behavior is also presented. No matter from which site the light is incident, as the g increases, the distribution of light at the output gradually becomes localized and eventually to a single spot at the initial site, evidently indicating the inhibition of optical tunneling. If the light is launched in the +1 site, the parabolic potential of the lattice sites on both sides are asymmetric, and the potential field difference between the +2 and +1 sites is significantly greater than that between the +1 and 0 sites, which results in stronger inhibition of light tunneling to the +2 site. If the light is launched in the 0 site, the potential field is arranged symmetrically, so the light intensity distribution on both sides is roughly the same. Since the potential difference between the +2 site and the nearest neighbor site is the largest and the light at the boundary site can only tunnel in one direction, the light is inhibited the most. Figure 3(a) (rightmost panels) shows the light field distribution diagrams at 9.6 mm in the +2 case, and the corresponding g are 0.16, 0.64, 1.44, and 3.3. Other cases are in Appendix D. From Fig. 4(d), when $g < 2$, tunneling is almost completely inhibited. Finally, subtle differences between different waveguides during the fabrication process would not significantly affect the results, according to the above experimental results. This is due to the advantage of the photonic lattice in the study of quantum mechanics, that is, more relaxed experimental conditions and strong robustness of physical effects.

TABLE I. Experimental data of Fig. 3(c).

	2.03 mm		4.35 mm		6.4 mm		8.35 mm		9.6 mm	
ε (π/mm)	I (arb. units)	σ	I (arb. units)	σ	I (arb. units)	σ	I (arb. units)	σ	I (arb. units)	σ
$\frac{2}{60}$	0.922	0.0057	0.773	0.0167	0.488	0.0042	0.300	0.0093	0.367	0.0031
$\frac{4}{60}$	0.944	0.0083	0.816	0.0071	0.661	0.0050	0.503	0.0111	0.346	0.0056
$\frac{6}{60}$	0.957	0.0022	0.877	0.0072	0.872	0.0029	0.869	0.0033	0.882	0.0072
$\frac{9}{60}$	1	0	0.977	0.0031	1	0	1	0	1	0

In conclusion, we have experimentally demonstrated the inhibition of optical tunneling, which arises from the parabolic potential caused by the twisting of the photonic lattices. Furthermore, our results show that the periodic potential imposing a constant inhomogeneous potential can be achieved by the specific geometric structure design of the photonic lattice. This would provide a unique 3D platform for studying quantum behaviors in experiments in complicated potential fields.

This paper is supported by the National Natural Science Foundation of China (Grant No. 12174222), Natural Science Foundation of Shandong Province (Grant No. ZR2021ZD02), and Taishan Scholars Program of Shandong Province.

APPENDIX A: HOPPING SYMMETRY OF THE WAVEGUIDE

We fabricate a series of two-waveguide systems to study the hopping symmetry of the structure of the waveguide, as shown in Fig. 5(a). The No. 1 waveguide is located at a depth of 230 μm below the surface. The interval of two waveguides is 15 μm. The No. 2 waveguide is arranged parallel to the No. 1 waveguide, and the angle θ changes from 0° to 330° at 30° intervals. Light with a wavelength of 633 nm is excited from the No. 1 waveguide. The light intensity at the output end of the No. 2 waveguide is shown in Fig. 5(b). We observe that, for different angles, the light intensity of the No. 2 waveguide is roughly the same, which shows that the fabricated waveguide has the same hopping rate in different directions. Figure 5(c) shows the light intensity distribution at the output facet at some angles. The excited site is circled by the bright white dotted line.

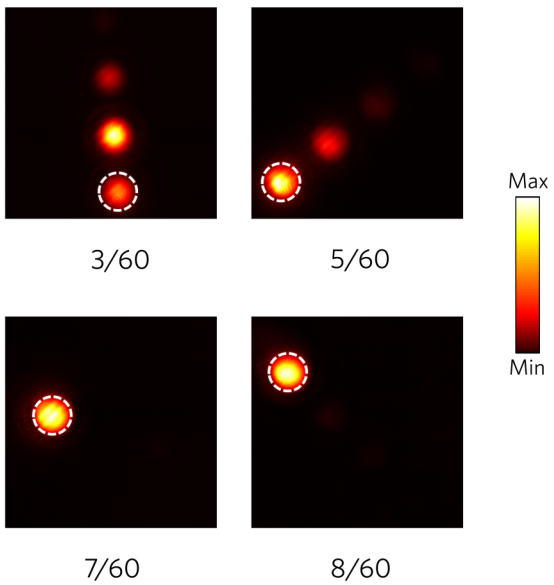


FIG. 8. Light intensity distribution with excited +2 sites. The lattice length is 9.6 mm. The rotating rates are $\frac{3}{60}$, $\frac{5}{60}$, $\frac{7}{60}$, and $\frac{8}{60}$ π/mm, respectively.

APPENDIX B: CALCULATION OF THE HOPPING RATE Δ

Since the fabricated waveguide arrays in Appendix A are consistent with the processing parameters of the twisted photonic lattice, we can use the results obtained above to calculate the hopping rate Δ. According to the results, as the propagation distance is 9.6 mm, the average light intensity at the No. 2 waveguide accounts for 79%. Figure 6 shows the relationship between the light intensity and the propagation distance obtained by calculation for $\Delta = 115\,\mathrm{m}^{-1}$. In this case, the proportion of the light intensity of the No. 2 waveguide is consistent with the experimental results at the output facet.

APPENDIX C: PERIODICITY OF LIGHT INTENSITY AT LONG DISTANCES

The light intensity at different rotating rates with a propagation distance of 40 mm is calculated. The light is excited at the +2 site. For the rotating rate ε from $\frac{2}{60}$ to $\frac{5}{60}$ π/mm, the light intensity has no periodicity with a length of 40 mm. For $\varepsilon = \frac{7}{60}$ π/mm, there are ~2 periods, and the period length is 9.3 mm. For $\varepsilon = \frac{8}{60}\pi$/mm, the period length is 7.1 mm. As the rotating rate increases, the distance that can maintain the

TABLE II. Experimental data of Figs. 4(b)–4(d).

	0		+1		+2	
G	I (arb. units)	σ	I (arb. units)	σ	I (arb. units)	σ
0.16	0.072	0.0021	0.098	0.0050	0.368	0.0031
0.36	0.134	0.0020	0.085	0.0020	0.412	0.0070
0.64	0.119	0.0071	0.0632	0.0028	0.346	0.0056
1.00	0.128	0.0027	0.189	0.0054	0.685	0.0051
1.44	0.399	0.0036	0.343	0.0038	0.882	0.0072
1.96	0.410	0.0158	0.482	0.0064	1	0
2.56	0.697	0.0054	0.612	0.0074	1	0
3.25	0.927	0.0029	0.913	0.0092	1	0

periodicity of the light intensity increases, and the length of the period decreases. For $\varepsilon = \frac{9}{60}\ \pi/\text{mm}$, periodicity almost always exists within a distance of 40 mm (Fig. 7).

APPENDIX D: LIGHT INTENSITY DISTRIBUTION IN OTHER CASES

See Fig. 8.

APPENDIX E: DETAILED EXPERIMENTAL DATA

The light intensity at the site in Figs. 3(c), 4(b), 4(c), and 4(e) is obtained according to the output intensity profiles taken by the charge-coupled device camera. Pictures are shown in Figs. 3(a), 4(a), and 8. The detailed data are shown in Tables I and II.

[1] C. Zener, Non-adiabatic crossing of energy levels, Proc. R. Soc. Lond. A **137**, 696 (1932).

[2] S. Longhi, Coherent destruction of tunneling in waveguide directional couplers, Phys. Rev. A **71**, 065801 (2005).

[3] M. Parto, H. Lopez-Aviles, J. E. Antonio-Lopez, M. Khajavikhan, R. Amezcua-Correa, and D. N. Christodoulides, Observation of twist-induced geometric phases and inhibition of optical tunneling via Aharonov-Bohm effects, Sci. Adv. **5**, u8135 (2019).

[4] S. Longhi, Control of photon tunneling in optical waveguides, Opt. Lett. **32**, 557 (2007).

[5] G. Della Valle, M. Ornigotti, E. Cianci, V. Foglietti, P. Laporta, and S. Longhi, Visualization of Coherent Destruction of Tunneling in an Optical Double Well System, Phys. Rev. Lett. **98**, 263601 (2007).

[6] Y. Luo, X. Wang, Y. Luo, Z. Zhou, Z. Zeng, and X. Luo, Controlling stable tunneling in a non-Hermitian spin-orbit coupled bosonic junction, New J. Phys. **22**, 093041 (2020).

[7] M. Aidelsburger, M. Atala, M. Lohse, J. T. Barreiro, B. Paredes, and I. Bloch, Realization of the Hofstadter Hamiltonian with Ultracold Atoms in Optical Lattices, Phys. Rev. Lett. **111**, 185301 (2013).

[8] S. Murmann, A. Bergschneider, V. M. Klinkhamer, G. Zürn, T. Lompe, and S. Jochim, Two Fermions in a Double Well: Exploring a Fundamental Building Block of the Hubbard Model, Phys. Rev. Lett. **114**, 080402 (2015).

[9] S. Longhi, Quantum-optical analogies using photonic structures, Laser Photon. Rev. **3**, 243 (2009).

[10] S. Longhi, Bloch dynamics of light waves in helical optical waveguide arrays, Phys. Rev. B **76**, 195119 (2007).

[11] S. Longhi, Light transfer control and diffraction management in circular fibre waveguide arrays, J. Phys. B: At. Mol. Opt. Phys. **40**, 4477 (2007).

[12] A. Szameit and S. Nolte, Discrete optics in femtosecond-laser-written photonic structures, J. Phys B: At. Mol. Opt. **43**, 163001 (2010).

[13] M. Heinrich, A. Szameit, F. Dreisow, R. Keil, S. Minardi, T. Pertsch, S. Nolte, A. Tunnermann, and F. Lederer, Observation of Three-Dimensional Discrete-Continuous *X* Waves in Photonic Lattices, Phys. Rev. Lett. **103**, 113903 (2009).

[14] Y. Plotnik, M. C. Rechtsman, D. Song, M. Heinrich, J. M. Zeuner, S. Nolte, Y. Lumer, N. Malkova, J. Xu, A. Szameit, Z. Chen, and M. Segev, Observation of unconventional edge states in 'photonic graphene', Nat. Mater. **13**, 57 (2014).

[15] C. Milian, Y. V. Kartashov, and L. Torner, Robust Ultrashort Light Bullets in Strongly Twisted Waveguide Arrays, Phys. Rev. Lett. **123**, 133902 (2019).

[16] Z. Shi, M. Zuo, H. Li, D. Preece, Y. Zhang, and Z. Chen, Topological edge states and solitons on a dynamically tunable domain wall of two opposing helical waveguide arrays, ACS Photonics **8**, 1077 (2021).

[17] Z. Zhang, R. Wang, Y. Zhang, Y. V. Kartashov, F. Li, H. Zhong, H. Guan, K. Gao, F. Li, Y. Zhang, and M. Xiao, Observation of edge solitons in photonic graphene, Nat. Commun. **11**, 1902 (2020).

[18] S. Mukherjee, A. Spracklen, D. Choudhury, N. Goldman, P. Ohberg, E. Andersson, and R. R. Thomson, Two Fermions in a Double Well: Exploring a Fundamental Building Block of the Hubbard Model, Phys. Rev. Lett. **114**, 245504 (2015).

[19] X. Zhang, V. A. Vysloukh, Y. V. Kartashov, X. Chen, F. Ye, and M. R. Belic, PT symmetry in nonlinear twisted multicore fibers, Opt. Lett. **42**, 2972 (2017).

[20] H. Zhong, Y. V. Kartashov, A. Szameit, Y. Li, C. Liu, and Y. Zhang, Theory of topological corner state laser in kagome waveguide arrays, APL Photonics **6**, 40802 (2021).

[21] Q. Yan, X. Hu, Y. Fu, C. Lu, C. Fan, Q. Liu, X. Feng, Q. Sun, and Q. Gong, Quantum topological photonics, Adv. Opt. Mater. **2021**, 2001739 (2021).

[22] M. C. Rechtsman, J. M. Zeuner, Y. Plotnik, Y. Lumer, D. Podolsky, F. Dreisow, S. Nolte, M. Segev, and A. Szameit, Photonic Floquet topological insulators, Nature (London) **496**, 196 (2013).

[23] T. Biesenthal, M. Kremer, M. Heinrich, and A. Szameit, Experimental Realization of PT-Symmetric Flat Bands, Phys. Rev. Lett. **123**, 183601 (2019).

[24] S. Mukherjee and R. R. Thomson, Observation of robust flat-band localization in driven photonic rhombic lattices, Opt. Lett. **42**, 2243 (2017).

[25] W. Song, Y. Chen, H. Li, S. Gao, S. Wu, C. Chen, S. Zhu, and T. Li, Gauge-induced Floquet topological states in photonic waveguides, Laser Photon. Rev. **15**, 2000584 (2021).

[26] S. Wu, W. Song, S. Gao, Y. Chen, S. Zhu, and T. Li, Floquet π mode engineering in non-Hermitian waveguide lattices, Phys. Rev. Research **3**, 023211 (2021).

[27] A. V. Zolotaryuk, P. L. Christiansen, and A. V. Savin, Two-dimensional dynamics of a free molecular chain with a secondary structure, Phys. Rev. E. **54**, 3881 (1996).

[28] W. F. Zhang, X. Zhang, Y. V. Kartashov, X. Chen, and F. Ye, Bloch oscillations in arrays of helical waveguides, Phys. Rev. A **97**, 063845 (2018).

[29] M. S. Petrovic, A. I. Strinic, N. B. Aleksic, and M. R. Belic, Rotating solitons supported by a spiral waveguide, Phys. Rev. A **98**, 063822 (2018).

[30] H. Zhong, R. Wang, F. Ye, J. Zhang, L. Zhang, Y. Zhang, M. R. Belić, and Y. Zhang, Topological insulator properties of photonic kagome helical waveguide arrays, Results Phys. **12**, 996 (2019).

[31] Z. Song, S. Liu, X. Gan, J. Zhao, and E. Li, Rotating properties of Bragg reflections and spatial solitons in rotating photonic lattices, Chin. Opt. Lett. **9**, 070801 (2011).

[32] K. Zhan, L. Dou, R. Jiao, W. Zhang, and B. Liu, Talbot effect in arrays of helical waveguides, Opt. Lett. **46**, 322 (2021).

[33] T. Yamakoshi, F. Saif, and S. Watanabe, Significantly stable mode of the ultracold atomic wave packet in amplitude-modulated parabolic optical lattices, Phys. Rev. A **97**, 023620 (2018).

[34] A. M. Rey, G. Pupillo, C. W. Clark, and C. J. Williams, Ultracold atoms confined in an optical lattice plus parabolic potential: a closed-form approach, Phys. Rev. A **72**, 033616 (2005).

[35] D. Tan, Z. Wang, B. Xu, and J. Qiu, Photonic circuits written by femtosecond laser in glass: improved fabrication and recent progress in photonic devices, Adv. Photonics **3**, 024002 (2021).

[36] F. Chen and J. R. V. de Aldana, Optical waveguides in crystalline dielectric materials produced by femtosecond-laser micromachining, Laser Photon. Rev. **8**, 251 (2014).

[37] D. Tan, X. Sun, Q. Wang, P. Zhou, Y. Liao, and J. Qiu, Fabricating low loss waveguides over a large depth in glass by temperature gradient assisted femtosecond laser writing, Opt. Lett. **45**, 3941 (2020).

[38] T. T. Fernandez, S. Gross, A. Arriola, K. Privat, and M. J. Withford, Revisiting ultrafast laser inscribed waveguide formation in commercial alkali-free borosilicate glasses, Opt. Express **28**, 10153 (2020).